Eur. Phys. J. B (2015) 88: 115
DOI: 10.1140/epjb/e2015-60021-x

THE EUROPEAN PHYSICAL JOURNAL B

Regular Article

Electron-related optical properties in T-shaped $Al_xGa_{1-x}As$/GaAs quantum wires and dots

J.C. Martínez-Orozco[1,2,a], M.E. Mora-Ramos[3], and C.A. Duque[2]

[1] Unidad Académica de Física, Universidad Autónoma de Zacatecas, Calzada Solidaridad esquina con Paseo la Bufa S/N, 98060 Zacatecas, Mexico
[2] Grupo de Materia Condensada-UdeA, Instituto de Física, Facultad de Ciencias Exactas y Naturales, Universidad de Antioquia UdeA, Calle 70 No. 52-21, Medellín, Colombia
[3] Centro de Investigación en Ciencias, Instituto de Investigación en Ciencias Básicas y Aplicadas, Universidad Autónoma del Estado de Morelos, Av. Universidad 1001, 62209 Cuernavaca, Mexico

Received 8 January 2015 / Received in final form 28 March 2015
Published online 7 May 2015 –

Abstract. The electronic structure and the intersubband optical absorption and relative refractive index change coefficients in T-shaped two-dimensional quantum dot and one-dimensional quantum wire are studied. The T-shaped quantum dot is embedded in $Al_xGa_{1-x}As$, with $x = 0.35$, the arm region has $x = 0$ whereas different values of the Al molar fraction are present for the T-stem region ($x = 0$, 0.7, 0.14, and 0.21). The model calculation is useful for studying both a 1D quantum wire of T-shaped cross-section and a 2D T-shaped quantum dot. The conduction and valence band states are described within the effective mass and parabolic band approximations. The agreement between calculated photoluminescence peak energy transitions and previously reported experimental values in such T-shaped quantum well wires is discussed. The electron-related optical coefficients are calculated using a density-matrix expansion with the inclusion of the linear and third-order nonlinear contributions to the dielectric susceptibility. The results for this optical response are presented as functions of the Al molar fraction, as well as of the polarization, and intensity of the incident light.

1 Introduction

Quantum confinement can be understood as the change in the electronic and optical properties of a system when it extends over a reduced-size region – usually a few tens of nanometers. Therefore, its essentials would depend not only on the dimensions but also on the geometric shape of the system. Arguably, among the seminal works in one-dimensional quantum carrier confinement, the article by Esaki and Tsu is one of the hallmarks [1]. Nowadays, the modern semiconductor experimental growth techniques allow for obtaining not only one dimensional quantum confining potential profiles, but also two- and even three-dimensional quantum confinement systems [2]. A particular example of one-dimensional (1D) quantum confined system is the charged carrier gas in a quantum well wire (QWW), which exhibits quantum confinement for its motion in the transversal region provided its dimensions are small enough, and free displacement along the axial wire direction [3]. As a consequence, this kind of structures are named as quasi-one-dimensional.

Quantum dots (QDs) are the archetype of quasi-zero-dimensional carrier systems. In these systems, quantum confinement prevents from free-like motion along any of the spatial directions. Therefore, the energy spectrum will be quantized and labeled by a set of three discrete quantum numbers [3]. However, if the conditions of fabrication make possible to highly reduce the dot's size along one of the directions – say z one – the influence of the confinement along it will be of much less importance, compared with that in-plane. One just needs to remember that for a sufficiently shallow one-dimensional potential well there will be only a single confined energy level. So, inter-level energy transitions would not be present for the – uncoupled – motion along the narrowest direction of the system and this can be considered as a two-dimensional quantum dot (2DQD).

Among the works devoted to the study of 2DQDs we can mention a number that deal with different symmetries. For example, in reference [4] the authors study a rectangular 2DQD. There, they reported the calculation of bound energy levels by using the transfer matrix method. More complex 2D geometries were considered by Ezaki et al. [5] in the study of the electronic properties of circular, elliptic, and triangular QD by means of a diagonalization procedure. Tiutiunnyk et al. [6] calculated the electronic structure as well as the intersubband optical properties

[a] e-mail: jcmover@fisica.uaz.edu.mx

for a triangular 2DQD. Along the same line, Martínez-Orozco et al. investigated the case of two coupled triangular 2DQDs, under the influence of a static electric field [7]. We can also mention a work in a parabolic 2DQD under the influence of external electric and magnetic fields as well as under hydrostatic pressure effects [8].

Here, we are interested in obtaining the electronic structure in $Al_xGa_{1-x}As/GaAs$ T-shaped heterostructures that show 2D confinement of charge carriers. This kind of profile is seen in QWW structures as those grown by Takahashi and collaborators [9]. In fact, this kind of structures was originally proposed by Chang et al. [10] in a report where the authors presented the energy level structure as a function of the quantum well thickness and proposed that such a system can be used to enhance exciton binding energies and optical properties by augmenting the oscillator strengths. Experimental reports on highly-confined T-shaped QWWs [11], and the analysis of carrier wavefunctions by magnetophotoluminescence in QWWs [12], were also published more than fifteen years ago. Also from the experimental point of view, there are several recent reports on this kind of T-shaped structures [13–15]. In particular, the work of reference [16] measures the low temperature photoluminescence as well as the temperature-dependent photoluminescence spectra for T-shaped dilute nitride quantum wires, in order to investigate their optical properties.

In the work, we are reporting the intersubband optical absorption coefficient as well as the relative refractive index change in T-shaped 2DQD. We have also calculated the photoluminescence peak energy transition in T-shaped QWW finding fairly good agreement with previously reported experimental results. The paper is organized as follows: Section 2 briefly presents the description of the theoretical model. In Section 3 one finds the corresponding results and discussion. Finally, Section 4 contains the main conclusions of the study.

2 Theoretical aspects

In this work we consider a T-shaped $Al_xGa_{1-x}As/GaAs$ structure which actually constitutes a 2DQD system [17]. Within the framework of the effective mass and parabolic band approximations, we have a conduction band electron with an effective mass m^*, confined within the T-shaped 2DQD. According with the experimental configuration reported by Takahashi et al. [9], we are considering the following potential profile:

$$V(x,y) = \begin{cases} V_0, \text{ if } (x,y) \notin \text{the T region}, \\ V_1, \text{ if } (x,y) \in \text{the T-stem region}, \\ 0, \text{ if } (x,y) \in \text{the T-arm region}. \end{cases} \quad (1)$$

This T-shaped 2DQD geometry is schematically depicted in Figure 1. It has an horizontal rectangular region – which corresponds to the T-arm region – made of GaAs of dimensions W_x-W_v and a T-stem region of $Al_xGa_{1-x}As$ semiconductor compound of dimensions W_h-W_y. In the present work, the values of W_v and W_h are taken from the experimental growth parameters reported in reference [9]. The T-shaped 2DQD is localized inside a rectangular region of $Al_xGa_{1-x}As$ where the confinement potential is $V(x,y) = V_0$. The confinement potential outside the rectangular region $L_x \times L_y$ is considered to be infinite. Calculation of confined states in the $x-y$-plane proceeds equally for both the QWW and QD cases. For symmetry reasons, the description of conduction band states in this 2D T-shaped structure is made using the Cartesian coordinate system. So that the 2D Hamiltonian will be:

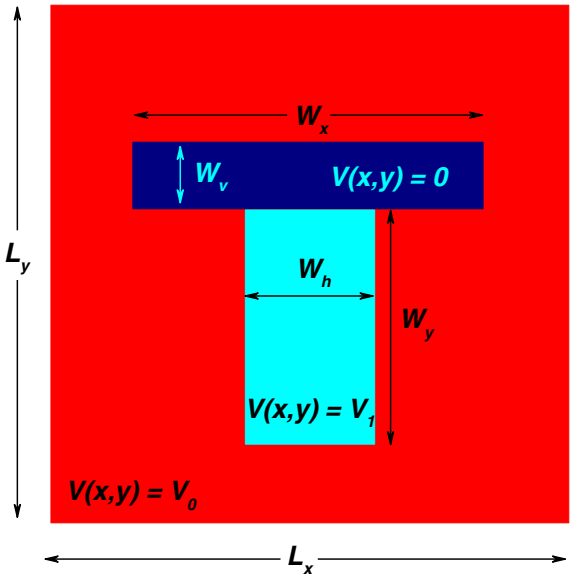

Fig. 1. Pictorial view of the potential profile for a T-shaped 2DQD of $Al_xGa_{1-x}As/GaAs$. The V_0 region has an Al concentration $x = 0.35$, and the T-stem region, of width W_h and height W_y, may have several smaller values of x. Finally the T-arm region, of height W_v and width W_x, is considered as made of GaAs. The dimensions of the structure have been taken from reference [9].

$$H = -\frac{\hbar^2}{2m^*}\left[\frac{\partial^2}{\partial x^2} + \frac{\partial^2}{\partial y^2}\right] + V(x,y)\,. \quad (2)$$

To solve the Schrödinger equation (2), we perform a diagonalization process that implies the expansion of the allowed quantum states over a complete set of orthonormal sinusoidal basis functions, arising from the solution of a 2D rectangular infinite potential well of sides $L_x \times L_y$. That is:

$$\Psi(x,y) = \frac{2}{\sqrt{L_x\,L_y}} \sum_{m,n} C_{m,n} \sin\left(\frac{m\,\pi}{L_x}\,x + \frac{m\,\pi}{2}\right) \times \sin\left(\frac{n\,\pi}{L_y}\,y + \frac{n\,\pi}{2}\right), \quad (3)$$

where $m = 1, 2, \ldots$ and $n = 1, 2, \ldots$ This proposal turns the problem of solving the differential equation into finding the eigensystem of an infinite Hamiltonian matrix. For practical purposes in our calculation we have considered

$$\alpha^{(3)}(\omega, I) = -\omega\, e^4 \sqrt{\frac{\mu_0}{\varepsilon_0\, \varepsilon_r}} \left(\frac{I}{2\, n \varepsilon_0\, c}\right) \frac{\rho \hbar\, \Gamma_{10}\, |M_{10}|^2}{[(E_{10} - \hbar\omega)^2 + (\hbar\, \Gamma_{10})^2]^2} \left\{4\, |M_{10}|^2 - \frac{|M_{11} - M_{00}|^2 [3\, E_{10}^2 - 4\, E_{10} \hbar\omega + \hbar^2(\omega^2 - \Gamma_{10}^2)]}{E_{10}^2 + (\hbar\, \Gamma_{10})^2}\right\} \quad (6)$$

225 terms in the expansion, which ensures a fairly good level of convergence for both the electron and heavy hole states.

With the information on both the electron and heavy hole energy states, calculated by means of the above discussed procedure, it becomes possible to determine the exciton photoluminescence peak energy transition. We can evaluate it from the expression $E_{PL} = E_{GAP} + E_0^e + E_0^h - E_B^X$, where E_{GAP} is the GaAs energy bangap, and E_0^e and E_0^h are the confined single particle ground state energies of the electron and heavy hole, respectively. In this sense, the calculation of heavy hole states follows the same procedure used for electrons with the appropriate changes in the effective mass and in the confinement potential. The term E_B^X corresponds to the exciton binding energy, which is mainly associated to the Coulomb correlation between the electron and heavy-hole carriers: $[V_C = -e^2/(\varepsilon_r\, r)]$, where e is the electron charge, ε is the GaAs static dielectric constant, and r represents the electron-hole distance. In order to find the exciton binding energy, in the present work we use a variational procedure by using a hydrogenic trial wave function given by:

$$\Phi(x_e, y_e, x_h, y_h, \rho_h, z) = N\, \Psi_0^e(x_e, y_e)\, \Psi_0^h(x_h, y_h) \times \exp(-\lambda\, r), \quad (4)$$

where N is the normalization constant,

$$r = \left[(x_e - x_h)^2 + (y_e - y_h)^2 + z^2\right]^{1/2},$$

and λ is the variational parameter. Here (x_e, y_e) and (x_h, y_h) are the electron and hole coordinates on the transversal section of the QWW and z is the relative coordinate along the growth direction. $\Psi_0^e(x_e, y_e)$ and $\Psi_0^h(x_h, y_h)$ are the ground state for the uncorrelated electron and hole carriers, respectively, associated with the corresponding Hamiltonian in equation (2). For details about the variational procedure to obtain the exciton binding energy in QWW, see for example [18–21].

The knowledge of the electronic structure also allows to calculate different elements of the optical response of the system when there is an incidental radiation of a given intensity and frequency. Among these quantities we have the electron-related optical absorption coefficient as well as the electron-related relative refraction index change. According to references [22,23], for small enough values of the incident light intensity (I), it is possible to use a procedure of solving the Von Neumann's equation for density matrix $\hat{\rho}$ based on a multi-order expansion. This allows to obtain expressions for first and third order electron-related optical absorption coefficient contributions; the latter one accounting for a nonlinear response. Accordingly, the first order intersubband optical absorption coefficient is given by:

$$\alpha^{(1)}(\omega) = \omega\, e^2 \sqrt{\frac{\mu_0}{\varepsilon_0\, \varepsilon_r}} \left[\frac{\rho\, \hbar\, \Gamma_{10}\, |M_{10}|^2}{(E_{10} - \hbar\omega)^2 + (\hbar\, \Gamma_{10})^2}\right], \quad (5)$$

whilst the third-order correction, due to radiation field – usually a laser one – effects of intensity I, is:

see equation (6) above.

So, the total absorption coefficient will be the sum of both linear and nonlinear ones. By following the same kind of approach it is straightforward to derive the coefficient of electron-related relative refractive index change for the system, this time working with the real part of the dielectric susceptibility. The linear contribution is then given by:

$$\frac{\Delta n^{(1)}(\omega)}{n} = \frac{e^2\, \rho\, |M_{10}|^2}{2\, n^2\, \varepsilon_0} \frac{E_{10} - \hbar\omega}{(E_{10} - \hbar\omega)^2 + (\hbar\, \Gamma_{10})^2}, \quad (7)$$

whereas the third-order correction is given by:

$$\begin{aligned}\frac{\Delta n^{(3)}(\omega, I)}{n} = &- \frac{\rho\, e^4\, |M_{10}|^2}{4\, n^3 \varepsilon_0} \frac{c\, I\, \mu_0}{[(E_{10} - \hbar\omega)^2 + (\hbar\, \Gamma_{10})^2]^2} \\ &\times \left[4(E_{10} - \hbar\omega)|M_{10}|^2 - \frac{(M_{11} - M_{00})^2}{E_{10}^2 + (\hbar\, \Gamma_{10})^2}\right. \\ &\times \left\{(E_{10} - \hbar\omega)[E_{10}(E_{10} - \hbar\omega) - (\hbar\, \Gamma_{10})^2]\right. \\ &\left.\left. - (\hbar\, \Gamma_{10})^2 (2\, E_{10} - \hbar\omega)\right\}\right]. \end{aligned} \quad (8)$$

Once again, the total relative change of the electron-related refractive index is obtained from the sum of these two contributions.

In the former equations, $E_{10} = E_1^e - E_0^e$ is the fundamental transition energy difference between allowed intersubband states, μ_0 the magnetic permeability of vacuum, ε_0 the free-space dielectric permittivity, and c is the speed of light in vacuum. The quantity Γ_{10} is the damping rate associated to the electron transition, which is equal to the inverse of the electron transition lifetime ($\Gamma_{10} = 1/T_{10}$). On the other hand, $n = \sqrt{\varepsilon_r}$ is the refractive index of the material in the active region of the structure.

A paramount parameter in these expressions is the dipole matrix element M_{fi}^w, defined as:

$$M_{fi}^w = \langle \Psi_f^e(x, y) | w | \Psi_i^e(x, y) \rangle, \quad (9)$$

being $\Psi_i^e(x, y)$ and $\Psi_f^e(x, y)$ the initial and final state wavefunction, respectively. In this expression $w = x, y$ represents the polarization of the incident light. In our study, the radiation can be considered x- or y-polarized. Here we must stress that, depending on the light polarization as

well as on the symmetry of the electronic wavefunctions, these matrix elements $|M_{fi}^{w}|$ would vanish or remain finite, thus giving rise to particular selection rules for the electron-related optical response, as a function of the T-stem region alloy concentration, as we will discuss in the next section.

3 Results and discussion

The results presented below are the outcome of a calculating procedure that considers a fixed geometric configuration, which coincides with that reported experimentally [9]. Clearly, the variation of the different lengths involved in the T-shaped region would also lead to additional dependencies of the calculated optical properties; but such an aspect, together with the possible influence of external probes, could be the subject of another work.

In our numerical computation we are considering an electron effective mass of $m^* = 0.067m_0$ (where m_0 is the free electron mass) and the relative dielectric constant of $\varepsilon_r = 12.5$. In our model we have a GaAs T-arm QW of width $W_x = 40$ nm and height of $W_v = 6$ nm, for the rectangular T-stem QW region, of $Al_xGa_{1-x}As$, of width $W_h = 14.15$ nm and height of $W_y = 14$ nm (see Fig. 1), assuming the possibility of varying the Al molar fraction x, as it was mentioned above. The whole T-shaped 2DQD is embedded within a region of $Al_{0.35}Ga_{0.65}As$. The Al-dependent potential barrier height for electrons is given by $V(x) = 0.6\ (1155\ x + 370\ x^2)$ in such a way that its height outside the T-region – denoted as V_0 in Figure 1 –, is of 270 meV. The potential barrier in the T-stem region obviously depends on the Al concentration. W_x and W_y have been chosen large enough in order to guarantee the convergence for the first 10 bound states.

With respect to the calculation of the optical coefficients, the input parameters taken into account for this system are: a transition relaxation time of $T_{10} = 0.2\times10^{-12}$ s and an electron density of $\rho = 3.8\times10^{22}$ m^{-3}. Here we must stress that this electron density corresponds to the situation of two electrons in the ground state – each one with different spin projection – distributed in a rectangular area of $L_x \times L_y$ and a height of 10 nm in this quasi-2DQW structure. Finally the laser intensity is varying from $I = 0.1$ to 0.3 MW/cm^2.

In Figure 2 we present the energy levels for the lowest six electron states in the T-shaped 2DQD when the Al concentration of the T-stem region goes from zero up to 0.25. For example when $x = 0$ we can report energies of $E_0^e = 27$, $E_1^e = 58$, $E_2^e = 72$, $E_3^e = 90$, $E_4^e = 96$, and $E_6^e = 113$ meV. Then, as the Al concentration rises, all the energy levels start to evolve towards higher values due to increment in the degree of electron confinement. Due to the two-dimensional nature of the carrier motion and the different rates of state variations, one may notice that the excited energy levels experience a set of anti-crossings when the Al fraction is below $x = 0.2$. Above that value all energies show a very smooth increasing monotony. The anti-crossing effect can be readily noticed when observing

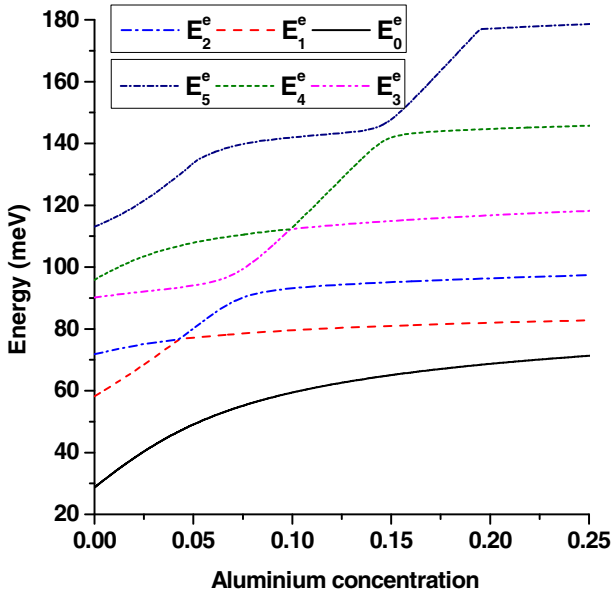

Fig. 2. Electron energy levels for the T-shaped 2DQD. Here are presented the energy levels as a function of the aluminium concentration in the T-stem region. It can clearly be observed several anti-crossing for the excited states until an aluminium concentration of 0.25.

the symmetry exchanges of the electron wavefunctions in the density plots that correspond to the four lowest confined states in Figure 3. It is also possible to observe that an increase of the Al contents above 0.15 almost leads to a complete confinement of these states within the T-arm region of the structure. This justifies the idea of its use as a kind of quantum well wire if the system would extend along the z-direction [16].

In order to compare our methodology with the available experimental data [9], in Figure 4 we give the calculated PL-peak energy, as a function of the Al concentration in the T-stem region. This curve corresponds to a transition from the ground state for the heavy holes E_0^h (considering an effective mass of $m_h^* = 0.34\,m_0$ and a band-offset of 40%) and the ground state for the electrons (the energy level structure for heavy-holes appear plotted in the inset of Fig. 4). In this analysis we have set the values $T = 5$ K, for the temperature, whereas the energy bandgap of GaAs is $E_{GAP} = 1519$ meV. In their experimental results, the authors reported that for an aluminium concentration $x = 0.07$ and $T = 5$ K there is a PL peak energy between 1581.7 and 1583.3 meV. Our theoretical results, represented by the black line, show the intersects with the absorption energy peak (blue line) when the aluminium concentration goes from $x = 0.0668$ to $x = 0.0728$ (see the two vertical red lines). Notice the good agreement between the theoretical and experimental findings.

A second round of comparisons with reports on PL measurements, this time for $Al_xGa_{1-x}As$ T-shaped QWWs of different sizes and compositions, is presented in Figure 5. Our results are compared with the reports by Soneya et al. [12] (lines I and II in the graphics) and Gislason et al. [11] (line III in the graphics). In order to

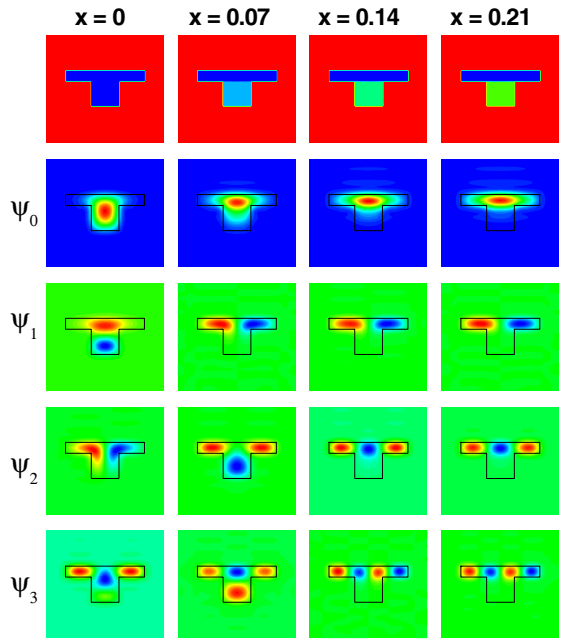

Fig. 3. Density plot of the wave function for the lowest four confined electron states in a T-shaped 2DQD. Each column corresponds to different values of the T-stem region aluminium concentration x. From left to right the values of x are 0, 0.07, 0.14, and 0.21.

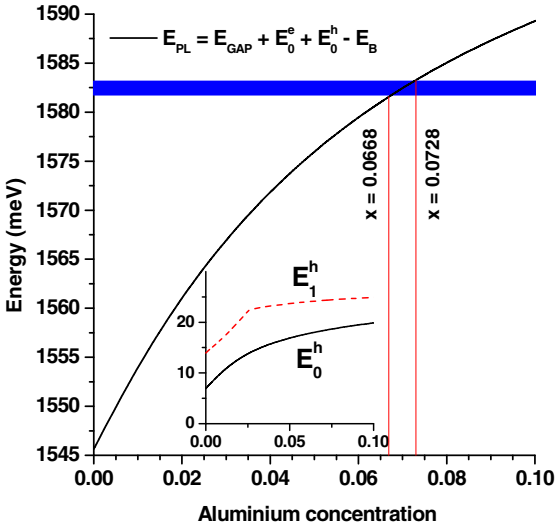

Fig. 4. Main photoluminescence peak energy transition (E_{PL}) as a function of the T-stem region aluminium concentration. In the inset, we plot the variation of the heavy-hole energies for the ground (E_0^h) and first (E_1^h) excited levels. The horizontal blue line (which width is 1.6 meV) represents the experimental finding by Takahashi et al. for $x = 0.07$ [9].

achieve coincidence, in I and II we have used 576 states in the expansion base (both for electrons and holes), whereas for the III case 625 states have been considered (both for electrons and holes) to reach the convergence of the calculations (changes in the PL-peak less than 0.1 meV).

The binding energies found for the structures I and II (11.8 meV and 17.9 meV, respectively, after the implementation of the variational calculation) are close to the results reported by Brown and Spector [21] and by Villamil et al. [24] in QWWs of circular cross-section. To make this particular comparison we have calculated an effective radius, corresponding to the region where the electron-hole pair is confined within the T-structure. Since the hole wavefunction is always more confined than the electronic one, we have assumed that there is at least a guarantee of 95% of electron confinement. By comparing the binding energy results of Figures 5I and 5II, it is possible to observe that E_b grows as a result of the increment in the T-arm size. This is consistent with the phenomenon of a greater localization of the electron wavefunction within the internal part of the heterostructure, widely observed in strongly confined systems.

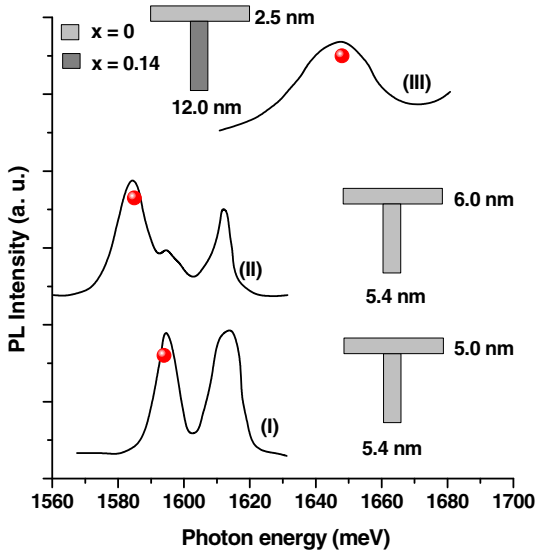

Fig. 5. Photoluminescence energy transitions in T-shaped quantum well wires. The solid lines correspond to experimental findings by Someya et al. [12] (lines I and II) and from Gislason et al. [11] (line III). In all cases the T-structure is surrounded by $Al_{0.3}Ga_{0.7}As$. In each case the T-structure is depicted with information of the aluminium contents and the sizes of the two wells. Also, for each case, the solid symbols correspond to our theoretical findings of the photoluminescence peak energy transition.

Going over the analysis of Figure 5III, in which the T-arm region has a much smaller size than the ones of the structures I and II, one notices that there is an additional confining effect due to the presence of a nonzero Al concentration in the T-stem region. Thus, we notice a significant increment in the binding energy (46.3 meV, arising from the variational) since the system tends to mimic that of an exciton confined within a QWW of rectangular cross section. In this case, our results are in close coincidence with those obtained by Degani and Hipólito [25]. Here, we have followed the same approach above mentioned to find the effective dimensions of the region within which the exciton is confined.

At this point, we have to mention that a truly realistic situation must take into account that the T-shaped

structures are usually grown considering three distinct crystal symmetry directions. That is, [001] for the z-axis, [110] for the y-direction, and $[1\bar{1}0]$ for the x-direction. Therefore, a more suitable calculation of the allowed energies should consider the anisotropy of the hole effective mass, and including the corresponding tensor components in the kinetic energy part of the Hamiltonian. Our procedure has been carried out assuming spherically symmetric masses. In addition, the approximation used sets the carrier masses as equal to the GaAs ones, throughout the whole structure (well and barrier potential regions). Such assumption is mostly correct when the dimensions of the structure are of the order of the exciton Bohr radius (11.7 nm in the GaAs by considering the electron-hole reduced mass to define the effective Bohr radius). However, in structures like the case III, the approximation is not good enough because the wavefunctions start having important contributions in the barrier regions. These elements are the possible restrictions to our estimation.

From now on we will restrain to take into account the properties of the ground and first electron excited state wavefunctions, since we are interested in the optical properties related to the main energy transition. If we go back to observe the corresponding – second and third – figure lines in Figure 3, it is readily apparent that both in the zero Al case and those of finite values of x, the ground and first excited state differ in symmetry with respect to either the horizontal (in the case of $x = 0$, there is a change in wavefunction sign of the first excited state when the vertical coordinate crosses a horizontal line at approximately the middle of the stem) or vertical directions (in the nonzero Al composition cases, the ground state wavefunctions are symmetrical with respect to the vertical line in the middle of the T-arm, whilst the first excite state wavefunctions are asymmetrical). All this has much to do with the optical response, under the conditions of a particular incident light polarization. To observe this in a more clear way, we are plotting in Figure 6 the magnitude of the diagonal and off-diagonal dipole moment matrix elements corresponding to intra- and inter-level transitions involving the E_0 and E_1 electron states. Both the x-polarization (Fig. 6a) and the y-polarization (Fig. 6b) of the incoming radiation have been considered. The results for the x-polarization are a complete consequence of the state symmetry in the problem. That is, the diagonal dipole moment matrix elements are zero throughout the entire range of Al concentration depicted due to the odd character of the integrand. The same phenomenon takes place in the case of the off-diagonal element while the Al molar fraction value lies below the anti-crossing point (see Fig. 3). Once the first excited state changes its symmetry for $x > 0.043$, the value of the element $|M^x_{10}|$ departs from zero.

In the situation of the incident light being linearly polarized along the y-direction, one finds a different context. Now the diagonal dipole moment matrix elements are practically nonzero throughout the considered interval of aluminium contents values. One notices a sharp increase of the $|M^y_{11}|$ and a sharp decrease of $|M^y_{10}|$ taking place

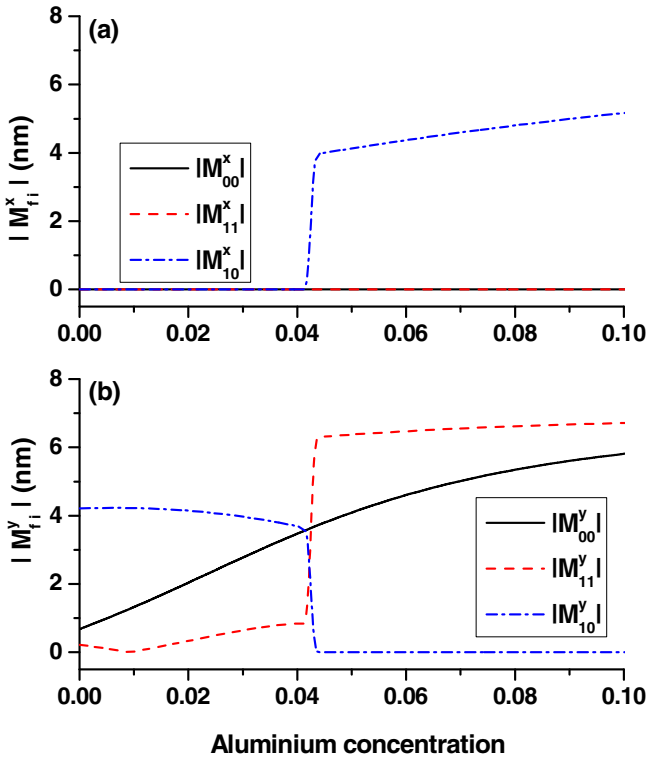

Fig. 6. Magnitude of the dipole matrix elements $|M^w_{fi}|$ as a function of the aluminium concentration in the T-stem region for: (a) x-polarized and (b) y-polarized incident light.

at the anti-crossing (when $x = 0.043$). All this, as it was above discussed is a consequence of the related features of the state wavefunction symmetries. With this information it is possible to discuss the results of the calculation of the electron-related optical coefficients considered.

In Figure 7a we present the linear, third-order nonlinear and total absorption coefficient in the case of y-polarized incident laser radiation of intensity $I = 0.1$ MW/cm^2 for three different values for the Al concentration in the T-stem region: $x = 0$, 0.02, and 0.04 (we need to keep in mind that for this particular polarization there will not be this kind of optical responses for $x > 0.043$, see the zero value of $|M^y_{10}|$ in Fig. 6b for this region of Al concentrations). We can observe that as the Al concentration x rises, the magnitude of the absorption coefficient diminishes, as it is clear from Figure 6b, and that the resonant peak initially experiences a slight redshift, with respect to the case of $x = 0$, for an aluminium concentration of 0.02 and then it experiments a blueshift for an aluminium concentration of 0.04. This can be accounted by observing the variation of the ground and first excited states depicted in Figure 2. In Figure 7b we have fixed the aluminium concentration in $x = 0$ and presented the effect of the increment in the incident laser intensity I for the values on the picture. As expected, the increase in photon intensity leads to the enhancement of the nonlinear contribution and, therefore, to a reduction of the total absorption response. However, we should remark that the features of α_{total} in Figure 7b, obtained for the higher

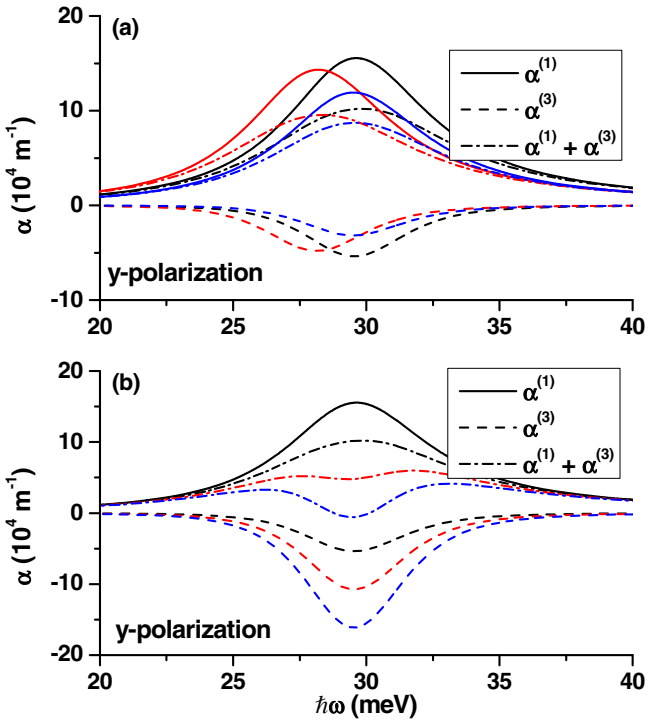

Fig. 7. Linear (solid line), third order correction (dashed line) and total absorption coefficient (point-dashed line) in the case of y-polarized incident light. In (a) the results are for $I = 0.1$ MW/cm^2 with several values of the Al concentration in the T-stem region: $x = 0$ (black line), 0.02 (red line), and 0.04 (blue line). In (b) we fixed the aluminium concentration $x = 0$ and several values of the laser intensity have been considered: $I = 0.1$ MW/cm^2 (black line), 0.2 MW/cm^2 (red line), and 0.3 MW/cm^2 (blue line).

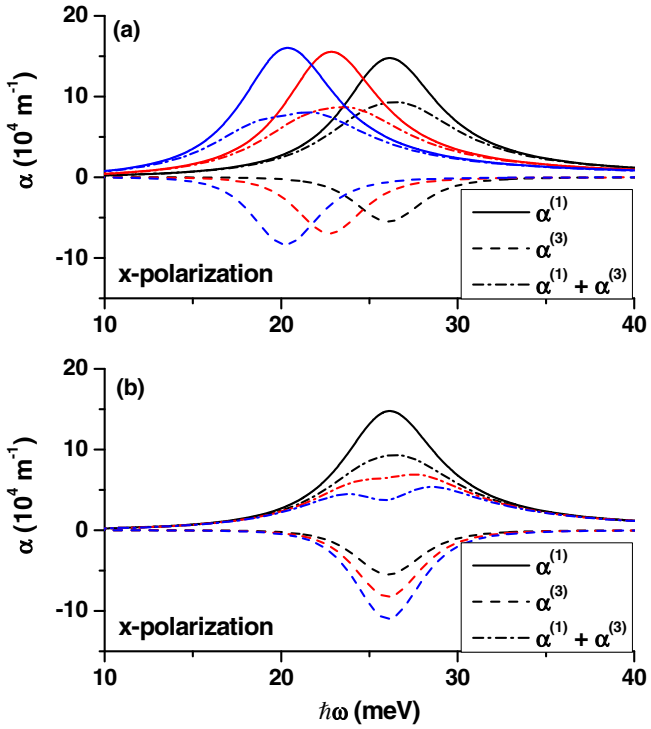

Fig. 8. Linear (solid line), third order correction (dashed line) and total absorption coefficient (point-dashed line) in the case of x-polarization. In (a) the results are for $I = 0.1$ MW/cm^2 with several values of the aluminium concentration in the T-stem region: 0.06 (black line), 0.08 (red line), and 0.10 (blue line). In (b) we have an aluminium concentration of $x = 0.06$ in the T-stem region and present the total absorption coefficient for several values of the laser intensity: 0.10 MW/cm^2 (black line), 0.15 MW/cm^2 (red line), and 0.20 MW/cm^2 (blue line).

values of I, reveal the known nonphysical – in this particular case – phenomenon of absorption bleaching which is nothing but the consequence of extending a perturbative treatment to a situation in which it is no longer correct [26]. Nonetheless, by observing the results depicted in Figure 7a, one can conclude that the appearance of the bleaching effect at a given value of I also depends on the Al molar fraction in the T-stem region.

In Figure 8 we present the absorption coefficient for three different values of the aluminium concentration. As seen above, there is not any optical response of the kind considered when we have x-polarized incident light for concentrations $x < 0.043$, so here we have chosen to show the outcome for $x = 0.06$, 0.08, and, 0.10. In this case we have found a redshift as the aluminium concentration rises, which can easily be explained by the energy level structure reported in Figure 2, in particular for concentration values above the anti-crossing one. Here we also observe a slight increment in the absorption coefficient resonant peak maximum that is directly related with the increase of $|M_{10}^x|$ (see Fig. 6a). Finally, in Figure 8b we plot the total absorption coefficient for zero Al concentration by considering laser field intensities of 0.10 MW/cm^2 (black point-dashed line), 0.15 MW/cm^2 (red point-dashed line) and, 0.20 MW/cm^2 (blue point-dashed line). In this figure we also plot the corresponding third-order corrections (dashed lines) and the linear absorption coefficient by a continuous black line as a reference.

Finally Figure 9 contains the corresponding relative refractive index change for (a) y-polarized incident light and (b) the x-polarized case, with $I = 0.3$ MW/cm^2. In the former case we compute this for the same set of aluminium concentrations used in the absorption coefficient computation: 0 (black line), 0.02 (red line) and 0.04 (blue line). Here we can easyly observe that the nodes for these properties correspond to the resonant peaks of the absorption coefficient and that the maximum (minimum) of the relative refractive index change is mainly modulated, as expected, by the magnitude of $|M_{10}^y|$. One also finds that third order correction is relatively small. On the other hand, in Figure 9b, the relative refractive index change is presented by considering a x-polarized incident light, for the same set of parameters as in the previous absorption coefficient computations. Provided the properties of the transition energy and the dipole moment matrix elements we find an analogous behavior. That is, we observe a redshift of the signal as well as a slight increment in its amplitude as we consider larger aluminium

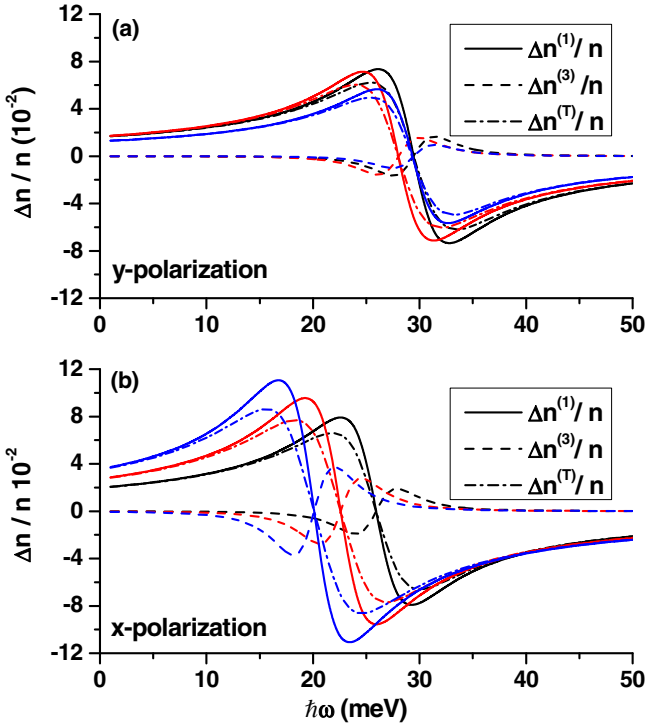

Fig. 9. Linear (solid line), third order correction (dashed line) and total relative refractive index change (point-dashed line) in the case of: (a) y-polarized light by considering three values of the Al concentrations in the T-stem region: $x = 0$, 0.02, and 0.04. In (b) we present this physical optical property but for aluminium concentrations of 0.06, 0.08, and 0.10 and x-polarization. In both plots the incident laser intensity is $I = 0.3$ MW/cm^2.

concentrations. Lastly we must stress that, in this case, the third-order correction is more important compared with the y-polarization configuration.

4 Conclusions

In this work we have addressed the investigation of the intersubband optical response in a $Al_xGa_{1-x}As/GaAs$ T-shaped 2DQD by calculating the absorption coefficient and the relative refractive index change. The various configurations considered differ in the value of aluminium concentration in the region that constitutes the stem of the T-like structure. It is shown that the amount of Al in this part of the system conditions the symmetry of the ground and first excited states wavefunctions and, therefore, the vanishing or non-vanishing of the optical coefficients depending on the orientation of in-plane linear light polarization. Augmenting the Al molar fraction within a rather small range of values reveals a redshift of the optical coefficients.

We have also carried out the calculation of the photoluminescence peak energy transition and compared the theoretical outcome with a previously reported experimental value of this quantity in T-shaped QWW, finding a satisfactory agreement.

J.C.M.O. acknowledges the Mexican National Council of Science and technology (CONACyT) for support through its program *Estancias Posdoctorales y Sabáticas al Extranjero para la consolidación de Grupos de Investigación* with number 207848 and also the *Universidad Autónoma de Zacatecas* for its grant for this sabbatical stay. J.C.M.O. is also grateful the *Universidad de Antioquia* for hospitality during his sabbatical stay. C.A.D. is grateful to the Colombian Agencies CODI-Universidad de Antioquia (Estrategia de Sostenibilidad 2014-2015 de la Universidad de Antioquia and projects: "On the way to development of new concept of nanostructure-based THz laser" and "Propiedades ópticas de impurezas, excitones y moléculas en puntos cuánticos autoensamblados"), Facultad de Ciencias Exactas y Naturales-Universidad de Antioquia (CAD-exclusive dedication project 2014-2015), and El Patrimonio Autónomo Fondo Nacional de Financiamiento para la Ciencia, la Tecnología y la Innovación, Francisco José de Caldas.
J.C.M.O. performed the full calculation of the uncorrelated electron and hole states and of the electron-related nonlinear optical properties. M.E.M.R. carried out the analysis and discussion of the obtained results, and C.A.D. was responsible of the comparison between the experimental and theoretical findings and of the implementation of the excitonic effects.

References

1. L. Esaki, R. Tsu, IBM J. Res. Dev. **14**, 61 (1970)
2. P.Y. Yu, Manuel Cardona, *Fundamental of Semiconductors: Physics and Materials Properties*, 4th edn. (Springer, 2010)
3. P. Harrison, *Quantum Wells, Wires and Dots: Theoretical and Computational Physics of Semiconductor Nanostructures*, 3rd edn. (Wiley, 2010)
4. E. Ata, D. Demirhan, F. Büyükklç, Physica E **62**, 71 (2014)
5. T. Ezaki, N. Mori, C. Hamaguchi, Phys. Rev. B **56**, 6428 (1997)
6. A. Tiutiunnyk, V. Tulupenko, M.E. Mora-Ramos, E. Kasapoglu, F. Ungan, H. Sari, I. Sökmen, C.A. Duque, Physica E **60**, 127 (2014)
7. J.C. Martínez-Orozco, M.E. Mora-Ramos, C.A. Duque, Physica B **452**, 82 (2014)
8. G. Rezaei, S.S. Kish, B. Vaseghi, S.F. Taghizadeh, Physica E **62**, 104 (2014)
9. Y. Takahashi, Y. Hayamizu, H. ltoh, M. Yoshita, H. Akiyama, L.N. Pfeiffer, K.W. West, in *Quantum Electronics and Laser Science Conference, QELS05* (IEEE, 2005), Vol. 1, p. 19
10. Y.-C. Chang, L.L. Chang, L. Esaki, Appl. Phys. Lett. **47**, 1324 (1985)
11. H. Gislason, W. Langbein, J.M. Hvam, Superlatt. Microstruct. **22**, 217 (1997)
12. T. Someya, H. Akiyama, H. Sakaki, Solid State Commun. **108**, 923 (1998)
13. D.H. Kim, J.H. You, J.H. Kim, K.H. Yoo, T.W. Kim, J. Nanosci. Nanotechnol. **12**, 5687 (2012)

14. P. Klangtakai, S. Sanorpim, R. Katayama, K. Onabe, Phys. Stat. Sol. A **207**, 1418 (2010)
15. P. Klangtakai, S. Sanorpim, F. Karlsson, P.O. Holtz, S. Pimanpang, K. Onabe, Phys. Stat. Sol. A **211**, 1740 (2014)
16. P. Klangtakai, S. Sanorpim, K. Onabe, J. Cryst. Growth **370**, 200 (2013)
17. R. Khordad, Opt. Quantum Electron. **46**, 283 (2014)
18. M.E. Mora-Ramos, M.G. Barseghyan, C.A. Duque, Physica E **43**, 338 (2010)
19. M.E. Mora-Ramos, M.G. Barseghyan, C.A. Duque, Phys. Stat. Sol. B **248**, 1412 (2011)
20. M.E. Mora-Ramos, C.A. Duque, Physica B **407**, 2351 (2012)
21. J.W. Brown, H.N. Spector, Phys. Rev. B **35**, 3009 (1987)
22. T. Takagahara, Phys. Rev. B **36**, 9293 (1987)
23. D. Ahn, S.-L. Chuang, IEEE J. Quantum Electron. **23**, 2196 (1987)
24. P. Villamil, C. Beltrán, N. Porras-Montenegro, J. Phys.: Condens. Matter **13**, 4143 (2001)
25. M.H. Degani, O. Hipólito, Phys. Rev. B **35**, 9345 (1987)
26. M. Załuźny, J. Appl. Phys. **74**, 4716 (1993)